Ultrasonics 147 (2025) 107527

Contents lists available at ScienceDirect

Ultrasonics

journal homepage: www.elsevier.com/locate/ultras

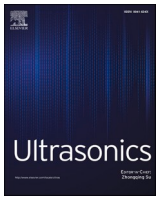

In-situ monitoring of μm-sized electrochemically generated corrosion pits using Lamb waves managed by a sparse array of piezoelectric transducers

C. Nicard [a,b], M. Rébillat [a,*], O. Devos [b], M. El May [b], F. Letellier [a], S. Dubent [a], M. Thomachot [c], M. Fournier [c], P. Masse [d], N. Mechbal [a]

[a] PIMM, CNAM / CNRS / Arts et Métiers Institute of Technology, Paris, France
[b] I2M, University of Bordeaux / CNRS / Arts et Métiers Institute of Technology, Bordeaux, France
[c] Cedrat Technologies, Meylan, France
[d] RESCOLL, Talence, France

ARTICLE INFO

Keywords:
Piezoelectric Transducers
Sparse Array
Pitting Corrosion
Structural Health Monitoring
Ultrasonic Lamb Waves
Controlled Electrochemical Experiments

ABSTRACT

Corrosion is a major threat in the aeronautic industry, both in terms of safety and cost. Efficient, versatile, and cost affordable solutions for corrosion monitoring are thus needed. Ultrasonic Lamb Waves (LW) appear to be very efficient for corrosion monitoring and can be made cost effective and versatile if emitted and received by a sparse array of piezoelectric elements (PZT). A LW solution relying on a sparse PZT array and allowing to monitor μm-sized corrosion pit growth on stainless 316L grade steel plate is here evaluated. Experimentally, the corrosion pit size is electrochemically controlled by both the imposed electrical potential and the injection of a corrosive NaCl solution through a capillary located at the desired pit location. In parallel, the corrosion pit growth is monitored in-situ every 10 s by sending and measuring LW using a sparse array of 4 PZTs bonded to the back of the steel plate enduring corrosion. As a ground truth information, the corrosion pit volume is estimated as the dissolved volume balancing the electronic charges exchanged during corrosion. The corrosion pit radius is additionally checked post-experiment precisely with an optical measurement. Measured LW signals are then post-processed in order to compute a collection of synthetic damage indexes (DIs). After dimension reduction steps, obtained DI values correlates extremely well with the corrosion pit radius. Using a linear model relating those DI values to corrosion pit radius, it is demonstrated that corrosion pit from 30 μm to 150 μm can be reliably detected, located, and their upcoming size extrapolated. Two independent experiments were achieved in order to ensure the repeatability of the proposed approach. LW managed by a sparse PZT array thus appears to be reliable and efficient to monitor growth of μm-sized corrosion pits on 316L steel plates. If embedded in aeronautical structure, such an approach could be a versatile and cost-effective alternative to actual non-destructive maintenance procedures that are time and manpower consuming.

1. Introduction

Corrosion within metallic structures can render an aircraft unairworthy by weakening structural components, roughening the outer surface, loosening fasteners, hastening cracking, and facilitating the entry of water into electronic fixtures. In 2016, the combined commercial aircraft fleet operated by European airlines was around 7900 airplanes. The annual corrosion cost for this number of aircraft was estimated by the US National Association of Corrosion Engineers to 2.2B $, which includes corrosion maintenance at 1.7B$ and downtime due to corrosion to 0.3B$. Anticipating corrosive conditions ahead of time can lead to significant cost savings and less aircraft downtime. It is estimated that savings between 15 % and 35 % of the cost of corrosion could be realized [1]. In order to limit corrosion issues, a typical aeronautic structure is made of qualified steel or aluminium alloys eventually protected from the environment by treating the surface with adequate coatings. It is generally expected that the protective surface is perfectly flawless over the whole structure. But on a large structure undergoing everyday service this cannot be the case. Impact damage during service life is a common occurrence of coating failure. Damage during maintenance (tools and split fluids) can also occur as well as paint cracking at high stress points around joints. From these initial premises, corrosion

* Corresponding author.
E-mail address: marc.rebillat@ensam.eu (M. Rébillat).

https://doi.org/10.1016/j.ultras.2024.107527
Received 10 July 2024; Received in revised form 29 October 2024; Accepted 19 November 2024
Available online 26 November 2024

pits can start and threaten the integrity of the structure at a global level, thus motivating the need for in-situ pitting corrosion monitoring technologies.

Industrially speaking, an ideal corrosion monitoring technology should allow to monitor large-scale structures, to automate measurements, to detect corrosion pits from their premises, and to exhibit a high correlation between sensors measurements and the size and locations of corroded areas. Although various effective non-destructive testing (NDT) methods have been developed to monitor corrosion [2,3,4,5], they remain limited in their ability to detect and assess corrosion premises and to reliably size a given corrosion damage. The first reason for that is *technological*. Eddy currents allow local monitoring (one side), are slow, difficult to calibrate, and remain a small-scale approach. Standard ultrasonic methods (A-scan and C-scan) are again small scale, rely on coupling fluid & human intervention and are thus rather slow. Optical methods (visual inspection, liquid penetrant) are large scale but can cope only with surface features that can be visually inspected and remain difficult to interpret. Radiography (X-rays, tomography) is small scale and relies on extensive hardware that cannot be used on the field. The second reason is *methodological*. Actual monitoring procedures are referred as planned maintenance and imply regular parts inspection by means of visual inspection and non-destructive testing through human highly qualified operators. Many of these inspections are (fortunately) unnecessary and as they rely on human intervention, their reliability is then subject to confidence intervals that establish a certain probability of detection. Moving from planned maintenance to condition based maintenance (CBM), *i.e.* maintenance only when necessary, seems mandatory to solve these issues. Monitoring in real time and autonomously the health state of structures is thus of high interest in this context. Such a process is referred to as Structural Health Monitoring (SHM) [6,7]. To achieve this goal, structures become *"smart"* in the sense that they are equipped with sensors, actuators, and algorithms that allow them to state autonomously regarding their own health. One can compare smart structures with the human body which, thanks to its various senses and nerves, is able to assess if it has been hurt, where it has been hurt, and to estimate how severe it is. Following this analogy, the SHM process is classically decomposed into four steps: damage detection, localization, classification, and quantification [8]. There is thus a real need for a large scale, automated, sensitive, low cost and embedded technology to develop corrosion monitoring SHM methodologies of aeronautic parts.

Ultrasonic technologies relying on Lamb Waves (LW) have been shown to be extremely sensitive to corrosion damage [9,10] and can be easily automated thanks to permanently embedded piezoelectric elements (PZT) networks [11]. In the present work, the focus is thus put on corrosion monitoring methods based on LW and applied experimentally to plate-like structures. Within that scope, some ultrasonic techniques are able to monitor very precisely corrosion damages using a single PZT but only locally around or below this element using either a strategy based on the time-of-flight [12,13], the CODA wave [14,15], or the electromechanical impedance [16,17]. These approaches are rather precise but can monitor only generalized corrosion phenomenon at the vertical of the PZT location thus limiting their practical use, apart from pre-identified hotspots to be carefully monitored. Another strategy that has been developed in the literature is based on dense arrays of PZTs elements (usually several tens of PZT) and aim at obtaining a tomographic image of the structure to be inspected using LW [18,19,20,21,22,23,24,25,26,27]. These approaches have been validated experimentally to localize and to size areas of several cm^2 suffering from generalized corrosion. A first drawback of those methods is that they require a large number of PZTs which makes them impossible to manage in practice and furthermore, they have not been validated on small μm-sized corrosion pits but only on large cm^2 generalized corrosion areas. A last strategy that has been explored relies on sparse PZT transducers arrays (*i.e.* arrays with less than 10 PZTs) and consists in computing features called damage indexes (DIs) from the measured signals and to infer corrosion damage information's from these DIs [28,29,30,31,32,33,34,35]. These approaches have been shown to be able to localize and to size generalized corrosion areas of several cm^2. From a practical perspective, they are more suitable for industrial development than the tomographic ones as they rely on fewer PZTs. Still, their performances on μm-sized corrosion pits remains unknown. In conclusion, LW inspection methods based on spare PZT transducers arrays are the most suitable from a practical point of view but have never been validated on small corrosion pits realistic of actual corrosion (from 10 μm to 150 μm) but rather on large generalized corrosion areas (in cm). The reason explaining the fact that it was yet not possible to generate a single corrosion pit in a controlled manner and to simultaneously and in-situ record LW interacting with such a damage. Consequently, the eventual sensitivity of LW to such small damages has never been demonstrated experimentally.

The generation of single localized corrosion pit on stainless steel with chloride ions has already been attempted in the literature. A first trial tried to simplify the problem by limiting the accessible surface for corrosion pits to initiate by using a steel wire or thin plate embedded in resin, letting only the smallest cross section possible accessible to corrosion [36,37]. This configuration is not appropriate here as a large sample is required to bond a sparse PZT network managing ultrasonic LW. Moreover, the obtained pit morphology was not realistic in these cases due to the presence of non-corroding resin at damages edges. Another approach consists in limiting the area where the chloride ions will react with the surface either by generating them very locally with Ag/AgCl probe [38] or by using micro-capillaries [39] sealed on the surface with silicon to prevent the NaCl solution to spread elsewhere on the surface. The use of Ag/AgCl probe is very effective to precisely initiate the pit but the size of pits generated this way is limited. The use of sealed micro capillary seems a good option to rapidly obtain confined condition due to the small volume accessible in the capillary and corrosion pits generated this way can easily be grown or stopped by respectively imposing drastic anodic or cathodic potentials. The fact that the capillary is sealed on the surface however remains an issue here as it will influence LW propagation and it makes direct optical observation during the experiment impossible. A last option is to protect the surface with a varnish, coat, or paint [40] except for a little area for the pit to develop. But again, the coating will impact LW propagation. Finally, the generation of single corrosion pits using non-sealed micro capillaries and without using varnish has been performed [41] where proper condition (concentrations and potential) allowing to create a single pit have been determined. However, corrosion pit generation was achieved on very small samples embedded in resin and in acidic conditions. This method, appears at the best starting point in term of methodology in the current context and has thus been adapted to fit requirements imposed by the simultaneous presence of a sparse PZT arrays managing LW emission and reception.

The objective of this paper is thus first to introduce an experimental setup allowing to control electrochemically the growth of a μm-sized corrosion pit and to simultaneously monitor it in situ by means of LW emitted and received using a sparse array of PZT transducers. It will secondly be demonstrated that such measurements can be post-processed to compute damage indexes (DIs) that, after dimension reduction, correlate very well with actual corrosion pit radius as estimated electrochemically. It is also shown that using a linear model relating DI values to corrosion pit radius, corrosion pit size from 20 μm to 150 μm can be reliably detected, located, and their upcoming size extrapolated.

The manuscript is then organized as follows. The experimental setup allowing for the electrochemical generation of controlled corrosion pits and in situ LW monitoring using a sparse array of PZT will be introduced in Section 2. Then, the signal processing steps allowing to compute DIs from the raw measurements of LW will be detailed in Section 3. Section 4 will then introduce the SHM methodology allowing to detect, localize and quantify corrosion pits damage size. Obtained results will be

discussed in Section 5 before drawing a general conclusion in Section 6.

2. Electrochemically controlled corrosion pits generations and in situ ultrasonic Lamb waves monitoring

2.1. Experimental samples

The experimental samples to be monitored are 1.5 mm thick 316L stainless steel samples of dimensions 80 mm by 125 mm. Four PZT transducers (Noliac NCE51, Ø10 mm × 1 mm) are bonded on the steel plate samples at specific geometrical positions provided in Fig. 1 [Left]. When choosing these positions, care has been taken to break symmetries when designing the 4 PZTs sparse array and not to be too close to the sample edges in order to limit LW reflections. A 150 mm coaxial cable is then brazed on each element to optimize the signal over noise ratio and to be able to send and receive LW. Finally, the PZTs are glued according to Cedrat Technologies bonding procedure. Two similar sample have been manufactured for this experimental campaign. Fig. 1 [Middle] and [Right] are showing the front and back faces of one of those two steel samples. The front face of the experimental samples (the one which will be corroded) was polished by hand with SiC grinding paper up to 1200 grade and after cleaned up with ethanol in order to prevent premature corrosion. To further avoid under joint corrosion, the area around the contact join between the sample and the corrosion cell that will be described afterwards is predetermined and varnished with an Acrylic Protective Lacquer (Electrolube). A non-varnished disc of ≃ 30 mm is let free at the centre where the corrosion pit damage will be generated afterwards.

2.2. Electrochemical experimental setup

A dedicated electrochemical cell (see Fig. 2 [Left]) has been designed and 3D printed with PETG filament for the purpose of the experiment. Dimensions of this cell are 96 mm × 60 mm × 48 mm for a volume of electrolyte of ≃ 150 mL. The specificity of this corrosion cell is the addition of a capillary guide that makes possible the insertion of a thin capillary through which corrosive species such as chloride ions can be injected. This capillary is in contact with the steel surface with a controlled angle (here 30° with respect to the surface normal) and is connected to a syringe pump (Pump 11 Elite, Harvard Apparatus) for injection speed control. The geometry of the cell also enables a direct optical microscopic observation of the steel surface with a VH-Z50L long focal objective Keyence. An overview of the whole experimental setup and of all the details is provided in Fig. 2 [Right].

In order to perform corrosion experiments, a standard three electrodes setup is used. The Working Electrode (WE) is the stainless 316L steel sample plate, the Counter Electrode (CE) is a 20 mm × 20 mm platinum grid-shaped wire, and the Reference Electrode (RE) is a silver chloride electrode (Ag/AgCl). The CE and RE are immersed in the electrochemical cell from the top and the steel sample (WE) is pressed with an adaptor on the bottom of the cell with an O-ring in order to keep water tightness while preventing any contact or mechanical stress on the PZTs. The electrodes are connected to a VersaSTAT 3F (Ametek) potentiostat that handles the electrochemical side of the experiment.

The aim of this setup is to generate corrosion on a small localised area close to the tip of the capillary (see Fig. 2) and to electrochemically control the dissolution rate in order to generate a pit with a controlled volume. Linear polarization curves are plotted in order to determine the experimental conditions allowing to control the kinetic of the localised steel dissolution.

Fig. 3 shows three polarisation curves corresponding to three different liquid electrolyte media in which corrosion can occur. The curve corresponding to the electrolyte without NaCl (S1 on Fig. 3) shows that the material has a passive behaviour in the whole domain of applied potential in that condition. The curve corresponding to the media with NaCl (S2 on Fig. 3) exhibits a drastic increase of the anodic current corresponding to the pitting potential above which corrosion occurs. In agreement with a previous work [41], the pitting potential measured for the higher NaCl 4 M concentration is lower than the one the lower NaCl 3 M concentration. These figures allowed to identify two potentials, $P1 = 150$ mV vs Ag/AgCl and $P2 = 400$ mV vs Ag/AgCl, respectively corresponding to a passive and a dissolution domain of the stainless steel in both NaCl concentrations. Table 1 summarizes information about the electrochemical behaviour of the stainless steel in the chosen electrolytes with and without NaCl.

2.3. *Controlled generation of localized corrosion damage*

In this section, the results obtained from two experimental conditions are detailed and discussed. For the first experiment, the electrochemical cell shown in Fig. 2 contains Na_2SO_4 0,1M aqueous solution (S1) and the 170 µm Ø capillary is connected to the syringe pump filled with a solution of Na_2SO_4 0,1M + NaCl 4 M (S2). The experimental results of this experiment I are represented in Fig. 4 on the left. The Fig. 4.I.1 shows the electrochemical potential measured versus time. At first the Open Circuit Potential (OCP) was measured during 30 min in order to reach a constant value corresponding to the passive behaviour of the 316L in the electrolyte. The measurement of the current shown in Fig. 4.I.2 confirms the passive property of the stainless steel with a very low stationary value that is measured for the current. After 30 min, the potential P2 was applied during 10 min without injection of chloride ions. The surface of the material continues to be passive as the same low current value as in OCP domain. This allows to validate the experimental conditions highlighted in Table 1. Next step consists in applying the

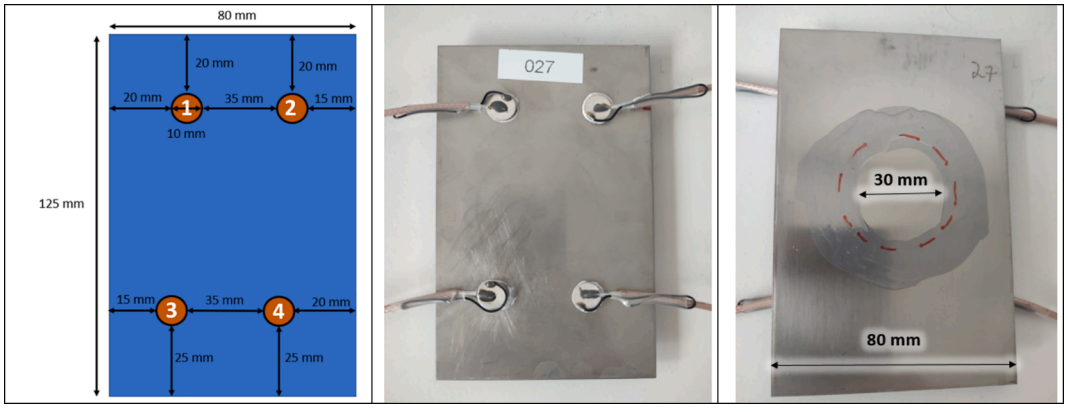

Fig. 1. Experimental steel sample under study. [Left] Position of the PZTs composing the sparse network. [Middle] Back face of the sample with the 4 bonded PZTs. [Right] Front face of the sample partially varnished before applying the corrosion cell.

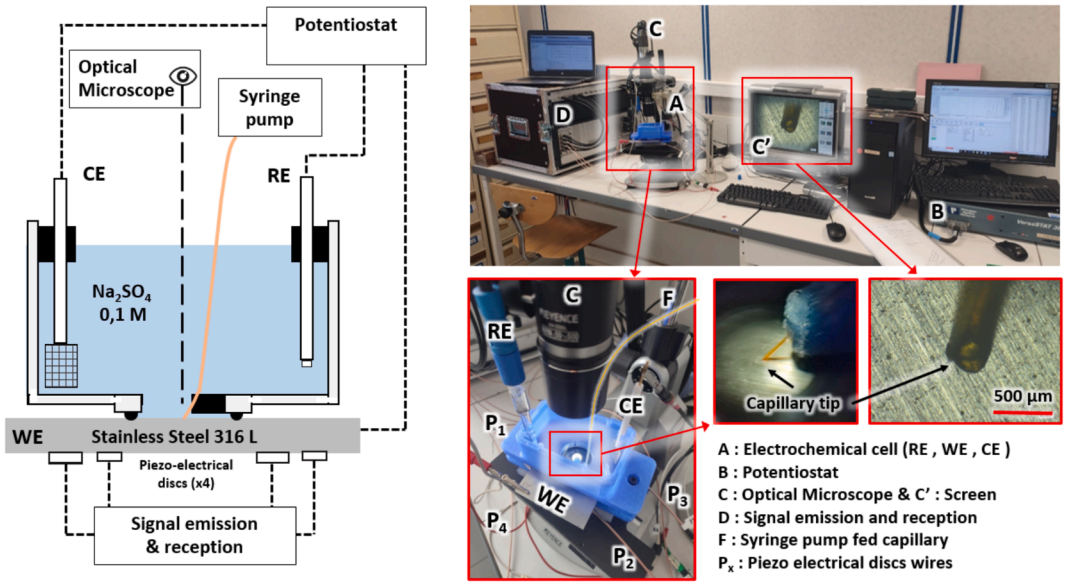

Fig. 2. [Left] Schematic of experimental set up and [Right] Pictures of experimental setup with zooms on the specific equipment's details in the text.

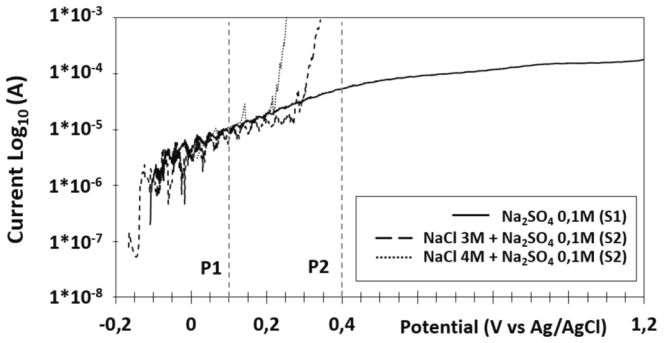

Fig. 3. Polarization curve of 316L stainless steel in various NaCl + Na_2SO_4 concentration, scan rate = 1.66 mV.$s^{-1.}$

Table 1
Corrosion behaviour of 316L depending on media (solution S1 and S2) and potentials (P1 and P2) applied.

	S1: Na_2SO_4 0.1 M	S2: Na_2SO_4 0.1 M + NaCl 3 M or 4 M
P1: 150 mV vs Ag/AgCl	Passive	Passive
P2: 400 mV vs Ag/AgCl	Passive	Active

potential P1 without injection of chloride ions. During this period, the material is still passive according to the information provided in Table 1. At time t_i the injection of the S2 solution through the capillary starts with a flow rate of 0.1 µL.s^{-1}. A few seconds after injection starts, the measured current increases which corresponds to a localised metallic dissolution in agreement with Table 1. Indeed, the chloride ions in the vicinity of the material's surface leads to local breakage of the passive film. Fig. 4.I.2 shows the cumulated electrical charge (mC) exchanged with the system versus time. While continuously and locally injecting chloride ions, the potential is alternated between P2 (growth of the pit) and P1 (stop of the metal dissolution). Note that the criteria for switching from P2 (active potential) to P1 (passive potential) is to approximately and successively reach 20, 60, 120 and finally 200 mC of cumulated electronic charge exchanged. During the time potential P1 is imposed, the current goes back to the low value corresponding to steel passive state and photographs are taken (see Fig. 4.a.b.c.d) in order to check damage size evolution before going back to potential P2 and continuing the damage growth.

A second experiment was performed where the concentration of NaCl was decreased to 3 M and the diameter of the capillary was increased to 220 µm (Fig. 4.II). The results are close to those of the first experiment and the slight differences between the two experiments will be investigated in the section in which the ultrasonic signals collected from the sparse PZTs array will be processed.

2.4. *Electrochemical dissolution ratio*

In order to calibrate this technique, *i.e.* in order to be able to link the charge exchanged during corrosion with the corrosion damage radius, a coefficient called *"dissolution ratio"* D_r ($mm^3.C^{-1}$) is defined as follows:

$$D_r = \frac{V}{Q} \tag{1}$$

where V is the volume of the pit formed by the dissolution of the steel when exchanging a charge Q during the experiment I and II presented in Fig. 4. This volume V is measured post-experiment using an optical microscope VHX-7100 objective Keyence. Fig. 5 [Left] shows a 3D optical topography obtained to compute the volume of the corrosion pit. Q is the final cumulated electrical charge as measured by the potentiostat at the end of the experiments in Fig. 4.I/II.3. Different couple of Q and V values obtained in the same condition for other experiments which were stopped at lower values of cumulated charges were compared and are plotted in Fig. 5 [Right].

A linear relationship linking the exchanged charge Q with the corrosion damage volume V was identified with a good value of regression correlation ($R^2 = 0.97$). This result shows that D_r could be considered as a constant coefficient whatever the pit radius in our experimental conditions. A value of $D_r = 18.4 \times 10^{-3}$ $mm^3.C^{-1}$ is given by the slope of the straight dotted line in Fig. 5 [Right].

From Eq. (1), an estimation of the radius of the corrosion pit r_p could be computed versus time by the following equation by assuming in a first approach that the pit has a hemispherical shape:

$$r_p = \sqrt[3]{\frac{3QD_r}{2\pi}} \tag{2}$$

with: Q corresponding to the cumulated electronic charge measured versus time (C).

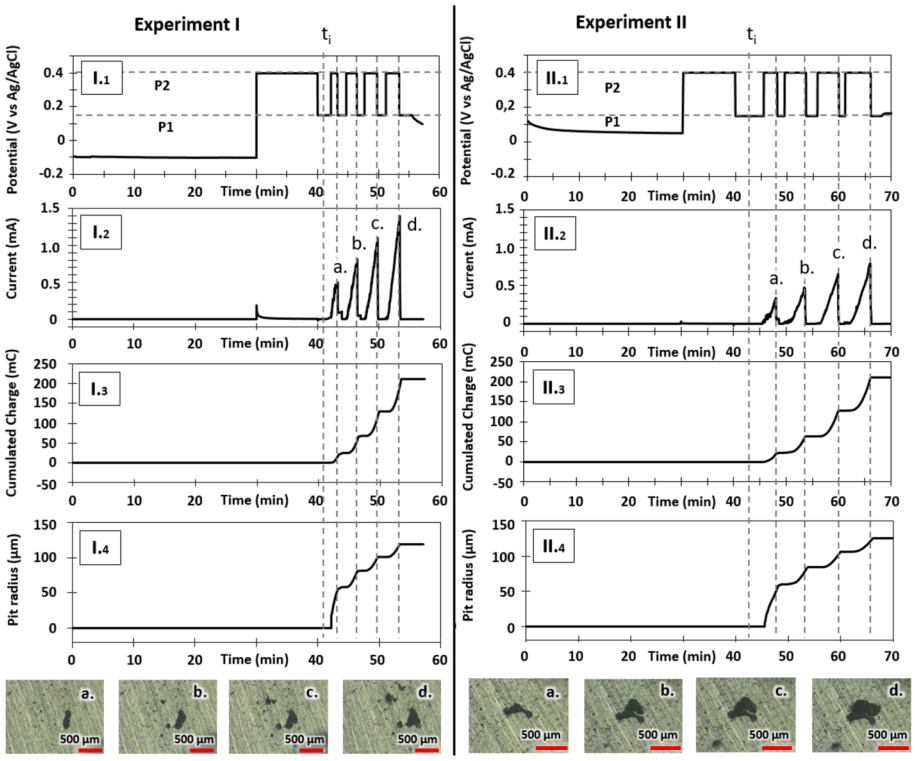

Fig. 4. Experimental measurement for localised corrosion on SS 316L. Those figures display the measured potential (−0.1), current (−0.2) cumulated electric charge (−0.3) and the calculated pit radius (−0.4) versus time. t_i: initial time of injection. (a, b, c, d): pictures from optical microscope at times given fig (I.2 and II.2).

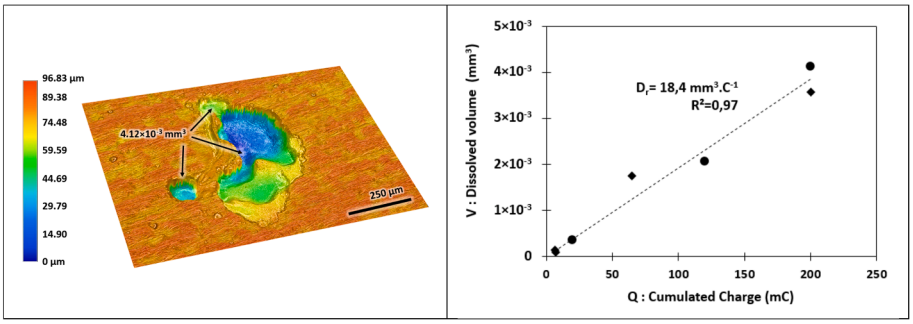

Fig. 5. [Left] Depth and volume measurements of the corrosion damage generated during experiment II (Fig. 4.II) by optical microscopy (Q = 211 mC). [Right] Volume of dissolved metal (V) as a function of cumulated electrical charge exchanged with the system (Q) after anodic polarisation at 0.4 V vs Ag/AgCl of 316L stainless steel plates in 0.1 M Na2SO4 + NaCl 3 M (◆) or 4 M (●).

The pit radius computed with Eq. (2) is plotted versus time for the two experiments in Fig. 4.I/II.4. Note that even if the pit is considered as a hemispherical hole in a first approximation, the final pit radius of 123 µm computed with $Q = 211$ mC in the experiment II, is within the same order of magnitude as that has been observed by optical microscopy in Fig. 5, thus justifying the proposed approach and the underlying assumption.

During the corrosion process, the corrosion damage simultaneously changes both in depth and in radius and the volume is here approximated to be hemispherical. Under the hemispherical assumption, if the radius is known, then the volume is also known and it is thus sufficient to specify only the damage radii to convey all the necessary information. Only the damage radius is provided in the following of the manuscript.

In both experiments, a localized corrosion damage has been generated and its growth has been controlled by electrochemistry. The dissolution ratio D_r will allow to estimate the volume of dissolved metal of the pit growing on the surface versus time from the measured of the electrical charge. The computed pit radius plotted in Fig. 4.I/II.4 can be used as a quantitative physical ground truth information for next part of this manuscript.

2.5. *In-situ ultrasonic Lamb waves measurements*

During the corrosion experiments described previously, LW are being emitted and received by the sparse array of 4 PZTs bonded at the back face of the steel sample enduring corrosion (see Fig. 1 [Middle]). The system used for LW management, provided by Cedrat Technologies, is denoted D in Fig. 2 [Right] and can be seen along with the whole experimental setup. This system is shown with more details in Fig. 6.

The LW management system is made up of three blocks with two of them begin conceived and designed by Cedrat Technologies [42,43,44]: the Generation Unit (GU) generates the signals to be sent for each channel and that can manage simultaneously up to 12 channels. The Lamb Waves Detection System (LWDS) can contain up to 16 independent channels. For each channel, the LWDS has a power amplifier (±15 V, 1A) allowing to drive the PZT with a bandwidth larger than 1 MHz,

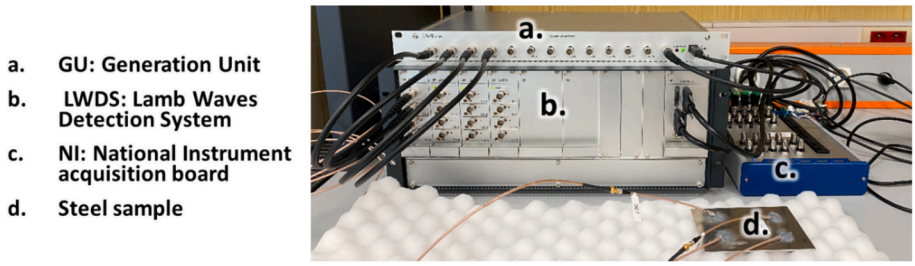

Fig. 6. Overview of Cedrat Technologies LW management system.

and a switching system allowing to toggle between emitting (pulse mode) and receiving (echo mode). Resulting signals are then acquired with a 2 MHz sampling frequency by a National Instrument (NI) acquisition board. Here, only 4 channels of the GU, the LWDS and the NI systems are being used. A custom MATLAB script configures in a round robin fashion one PZT in actuator mode (pulse mode) and the three others in sensing mode (echo mode) before performing the acquisition. The PZT in pulse mode will generate a Lamb wave at a central frequency of 200 kHz and the other ones will receive the resulting LW that will then be measured by the NI interface. The time required to collect ($\simeq$ 50 ms) and store ($\simeq$ 9.5 s) the signals for the 4 PZT is around 10 s. Measurements are run constantly during the corrosion process and thus one measurement is available roughly every 10 s during the corrosion pits growth. Precise time stamps associated with each measurement are also stored. Raw experimental data are available in Open Access [64].

3. Optimal damage indexes computation from Lamb waves measurements

3.1. Denoising of raw Lamb waves signals

As pre-processing steps, the measured LW signals are first denoised by means of a discrete wavelet transform up to the order 4 using the *"db40"* wavelet. Those signals are then filtered around their excitation frequency $f_0 = 200$ kHz using a continuous wavelet transformation based on *"morlet"* wavelets and with a scale resolution equal to 20. The objective of this pre-processing step is to perform a band pass filtering around the excitation frequency by means of wavelets in order to limit the influence of experimental noise. The scale parameter can be sought as an image of the bandwidth of the retained bandpass filter over the frequency range of interest. Here, choosing it equal to 20 is something relatively common and provided convenient results in past studies [45,46,47]. The diaphonic part present in the measured signals (*i.e.* the copy of the input signals that appears on the measured signal due to electromagnetic couplings in wires) has been eliminated based on the knowledge of the geometrical positions of the PZT and of the estimated waves propagation speed in the material.

Examples of LW signals measured on the path going from PZT 1 (actuator) to PZT 2 (sensor) (see Fig. 1 [left]) for both experiments and for various radius of the corrosion pits are shown in Fig. 7. From this figure, it can firstly be seen by comparing the left and right ones that even if the two steel samples were assumed to be similar, it appears that the LW signals corresponding to a given path on those samples do no convey similar LW signals. This can be attributed to the fact that small discrepancies still exists between samples due to the bonding or the positioning of PZT that can slightly differ and thus produce different LW signals.

Furthermore, for both experiments, it appears that the collected LW signals are not changing that much when the corrosion pit size is increasing and look rather similar. Experimentally, the effects of such small corrosion pits on recorded signals are thus expected to be subtle and of small amplitude on the LW measured signals. The differences between the Lamb waves signals collected in the healthy condition (with a radius equals to 0 μm) and the ones collected at various corrosion states (with a radius larger than 0 μm) are shown in Fig. 8. This indeed confirms that the diffraction generated signals are of small amplitude, but still exists and can be experimentally observed.

3.2. Damage indexes computation

After LW signals have been denoised for all available actuator-sensor paths, signals are compared together one by one through the computation of a set of 40 Damage Indexes (DI) that have been previously designed for damage monitoring purposes [48]. The mathematical details regarding the computation of these DIs are provided in Appendix. These DIs can be categorized depending on the feature of the signal that they target to describe (energy, amplitude, time of flight, or statistical properties among others). One DI is computed from two signals that one would like to compare. Typically one signal in a healthy or reference state is compared to another in a damage state. However, as it has been previously shown, the signals due to the corrosion pit may be of small amplitude and thus corrupted by noise. In order to mitigate that issue, Lamb waves measurements are repeated several times when it is possible (here in the healthy reference state and when the injection is stopped and thus the corrosion pit radius steady). Consequently, instead of having one value of a DI, several values associated with its probability density function are available.

As detailed in Section 2.3, several steady states values of corrosion

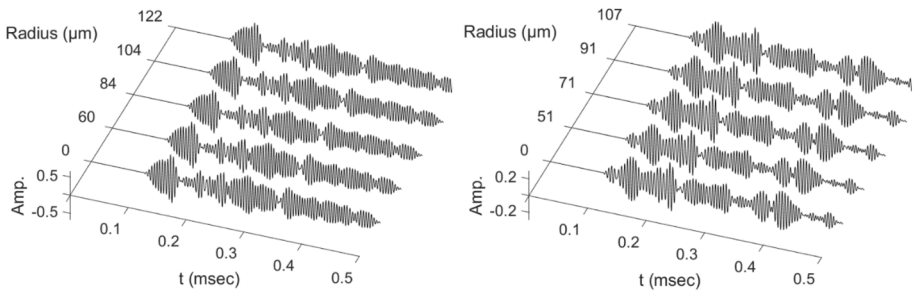

Fig. 7. Example of LW signals measured on the path going from PZT 1 (actuator) to PZT 2 (sensor) for the first [left] and second [right] experiments and for various radius of corrosion pits.

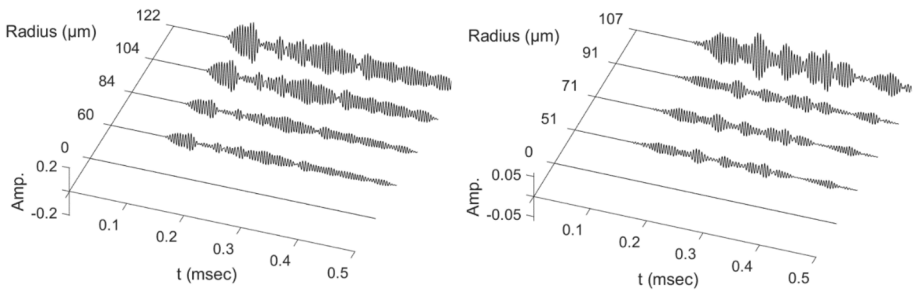

Fig. 8. Example of the difference between healthy and damageLW signals measured on the path going from PZT 1 (actuator) to PZT 2 (sensor) for the first [left] and on the path going from PZT 2 (actuator) to PZT 3 (sensor) for the second [right] experiment and for various radius of corrosion pits.

pit radius are reached when the injection of NaCl is stopped. As a first way to compute DIs, signals are grouped with respect to these steady state values of corrosion pit radius. Thus, for each experiments, 5 groups of signals are available and corresponds either to a reference state (no corrosion) or to a given corrosion state (given corrosion radius, see Section 2.3). Given N signals being available for a given corrosion state, for the *"reference* versus *corrosion"* configurations, N^2 DIs can be computed (N reference signals versus N corrosion ones), and only $N \times \frac{N-1}{2}$ DIs for the *"reference* versus *reference"* comparison configuration, because redundant comparisons within the N available repetitions are discarded. Illustrative DIs histograms (namely cross-correlation [CC] and standard deviation [STD]) for the reference and corrosion cases corresponding to intermediary corrosion pits radius values for the path *"Actuator 1 − Sensor 3"* are plotted in Fig. 9. From this figure it can be seen that irrespectively to the considered experiment or to the considered DI, a global increase is observed along with the corrosion pit radius growth. Furthermore, it can also be seen that the DIs distribution for a given case is relatively spread around its mean value meaning that the effect of noise is somewhat important here and should be considered. This is in agreement with the previously observed small effect of corrosion pits on the measured LW signals. This however demonstrates the effective experimental sensibility of the LW based proposed approach to µm-sized corrosion pits.

A second way to compute DIs consists in processing incoming LW measurements acquired sequentially each $\simeq 10$ s and not to group them as previously. A first measurement is taken as a reference and then all the upcoming measurements are compared to this reference one and associated DIs computed. In that case, the obtained DIs thus constitute temporal series evolving with time along with the damage radius shown in Section 2.3. The correlation of some DIs (namely cross-correlation [CC] and standard deviation [STD]) with corrosion pit radius for the path *"Actuator 1 − Sensor 3"* are plotted for both experiments on Fig. 10. The plateaus associated with each state corresponding to a stop in the corrosion process can clearly be seen on this figure. The correlation quality between the DIs and the corrosion pit radius can be evaluated using the R^2 coefficient denoting the goodness of fit: a value close to one indicates a very good correlation and a value close to zero a very bad one. From this figure, it can thus be seen that whatever the considered DIs or the considered experiment, an acceptable correlation between DI values and corrosion pit radius is indeed observed. This correlation is

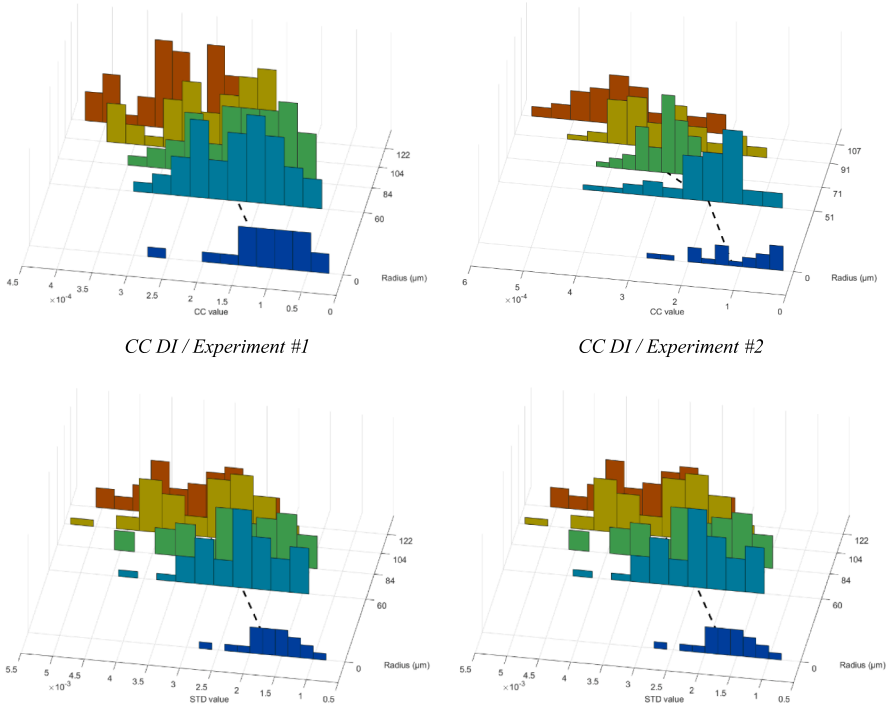

CC DI / Experiment #1 *CC DI / Experiment #2*

STD DI / Experiment #1 *STD DI / Experiment #2*

Fig. 9. Example of the evolutions with corrosion radius size of DIs CC [Top] and STD [Bottom] computed for the first [Left] and second [Right] experiments for the path PZT 1 to PZT 3.

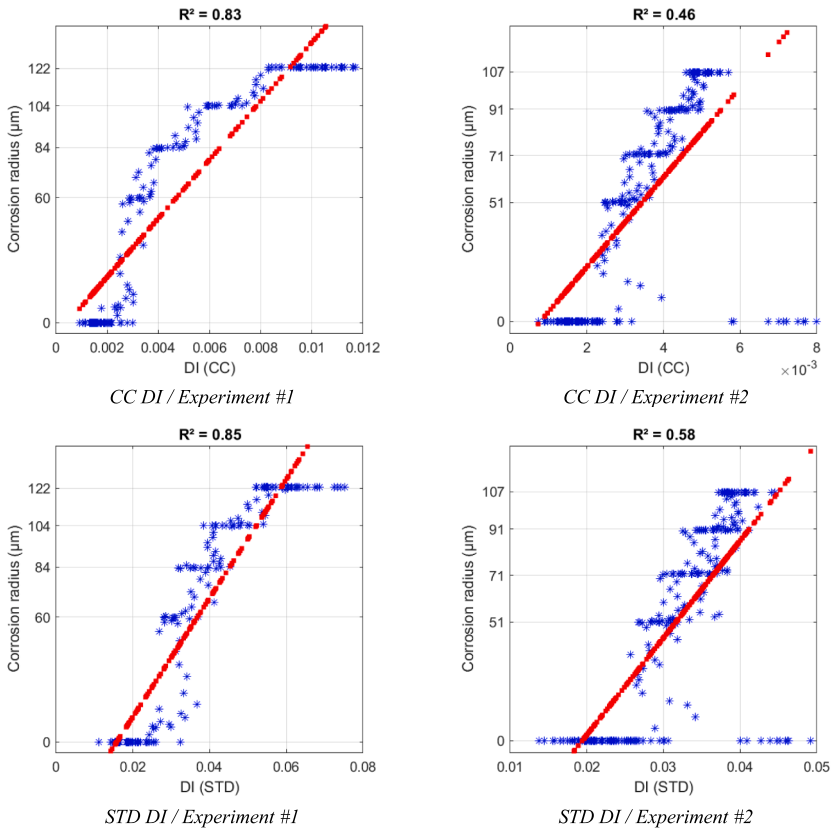

Fig. 10. Example of the correlation with corrosion radius size of DIs CC [Top] and STD [Bottom] computed for the first [Left] and second [Right] experiments for the path PZT 1 to PZT 3.

high in the first experiment and lower for the second experiment for the chosen DIs. Finally, all the DIs evolve in a monotonic and increasing manner with corrosion pit radius, and this evolution can be roughly qualified as linear.

3.3. Dimension reduction

As at be shown previously, it is possible to compute from the measured LW signals a set of 40 DIs conveying potential information regarding the corrosion pit damages to be monitored. Such DIs can be computed for any path between one PZT used as an actuator and another one used as a sensor. It is then necessary to be able to reduce the dimension of this set of informative DIs in order to filter out as many variability effects as possible and to keep the most information possible regarding corrosion pit sizes.

As a first dimension reduction step, the DIs are integrated spatially over the structure to be monitored. A given DI denoted DI_{nm} can be computed for any path joining a PZT element n considered as an actuator and a PZT element m considered as a sensor. What has been chosen here is just to sum out the damage indexes obtained for all the paths in order to obtain a global damage index denoted DI_G. As a given PZT cannot be simultaneously an actuator and a sensor (this is possible in pule echo mode that is not available here), only the terms with $m \neq n$ are kept in the summation. In order to integrate this information across the whole structure to be monitored (here across the whole steel sample on which a 4 PZT sparse network is bonded), the global DI denoted DI_G will be computed as follows:

$$DI_G = \sum_{n=1}^{4} \sum_{m \neq n} DI_{mn} \tag{3}$$

As a second dimension reduction step, the 40 DIs that have been computed previously can be processed in order to compute a single DI being the most informative possible. Traditionally, Principal Component Analysis (PCA) has been used as a dimension reduction technique to investigate whether the information contained within the DIs can be condensed to a lower dimensional space [49]. However, as reported in [50], the aim of PCA is to find directions that explained the maximum of variance in the input data. One should here recall that in addition to input data (40 DIs), output data are also available (corrosion pit size), and the dimension reduction problem can be set up in a supervised manner. In order to achieve this goal, some alternate methods have been proposed such as Partial Least Squares (PLS) and Canonical Correlation Analysis (CCA) [51,52,53] that seek for a lower dimensional space optimizing discrimination. The CCA approach looks for the linear combination of DIs that maximizes the correlation between projected input and output data. In this way, CCA can conveniently deal with directions of the input or output spaces that present very high variance, and that would therefore be over-emphasized by PLS, even if the correlation between the projected input and output data is not very significant. The CCA method has thus been selected to achieve the final dimension reduction step here. Consequently, after spatially integrating data over the whole structure according to Eq. (3), a second dimension reduction operation is achieved from a DI space having 40 dimensions to a reduced mono-dimensional space using CCA and makes use of both the 40 DIs and the corresponding corrosion pit sizes (as CCA is a supervised method) for learning.

The DIs after the two dimension reduction steps and for the cases where corrosion was stopped at given corrosion radius values are shown in Fig. 11. From this figure it can be seen that the dimension reduction steps allow to considerably lower the variability within each group and also to enhance the differences between groups, thus allowing for potentially better monitoring abilities of corrosion radius damage.

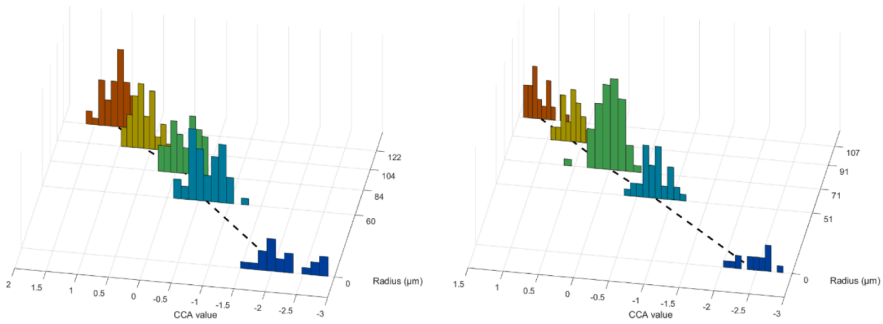

CCA DI / Experiment #1 *CCA DI / Experiment #2*

Fig. 11. Example of the evolutions with corrosion radius size of DIs CCA computed for the first [Left] and second [Right] experiments.

Furthermore, the correlation between the reduced DIs obtained after spatial integration and CCA and actual corrosion pits sizes are shown in Fig. 12 for both experiments. In this figure, it can be seen that the correlation quality after dimension reduction is close to 1 and thus extremely satisfying for both experiments, much more that when using the original DIs. Consequently, achieving the dimension reduction steps by spatial integration and by means of CCA appears here to be very relevant here as it allows to build an extremely good features allowing to potentially predict the corrosion pit size. The same observation has been made for the two experiments which strengthens those conclusions. A linear model relating CCA to actual corrosion pit size will thus be retained in the following.

4. Corrosion pits SHM monitoring strategy

The question that arises now is how to take benefits of this reduced dimension DIs and of this linear correlation with corrosion pit radius size for structural health monitoring (SHM) purposes. This question will be addressed here through the analysis of three consecutive SHM steps, namely damage detection, damage localization, and finally damage size extrapolation.

4.1. Damage detectability

Damage detection is related to the ability of distinguishing between the presence or the absence of a corrosion pit with a given probability of false alarm (PFA). In order to achieve this goal, one solution consists in fitting an analytical probability density function (PDF) to the data collected in the reference state, and to compute a DI threshold ensuring a given PFA chosen a priori [54]. Then, in order to infer which minimum corrosion pit size can be detected with the proposed approach, a PDF for the corroded case can also be established that depends linearly on the corrosion radius. Finally, the minimum corrosion radius that can be detected with a given probability of detection (POD) chosen a priori can be determined as will be shown in what follows.

The PDF $p(DI|r)$ denoting the probability of having a DI equal to DI with a corrosion radius of r is assumed to be Gaussian with a constant standard deviation σ and a mean $\mu(r) = \mu_0 + \alpha r$ increasing linearly with corrosion pit radius according to the linear correlation demonstrated previously between CCA and corrosion pit radius. For each experiments, the standard deviation σ as well as the parameters governing the evolution of the mean (μ_0 and α) can be estimated using the DI histograms shown in Fig. 11. The PDF model is plotted along the actual DI distributions for both experiments in Fig. 13. From this figure, it can be seen that the simple models correctly describe the probabilistic nature of the experimental DI distributions observed for both experiments. This model can be formally written as in Eq. (4).

$$p(DI|r) = \frac{1}{\sqrt{2\pi}\sigma} exp\left[-\frac{(DI - (\mu_0 + \alpha r))^2}{2\sigma^2} \right] \tag{4}$$

In this model, the PDF associated with a healthy or reference state can be simply written as $p_H(DI) = p(DI|r = 0)$ and the PDF associated with a damaged stage with a corrosion pit of size R corresponds to $p_D(DI, R) = p(DI|r = R)$. Consequently, for a given DI threshold T that has been previously selected for corrosion pit damage detection purposes, the PFA can be computed as in Eq. (5).

$$PFA(T) = \int_T^{+\infty} p_H(DI) dDI = \int_T^{+\infty} p(DI|r = 0) dDI \tag{5}$$

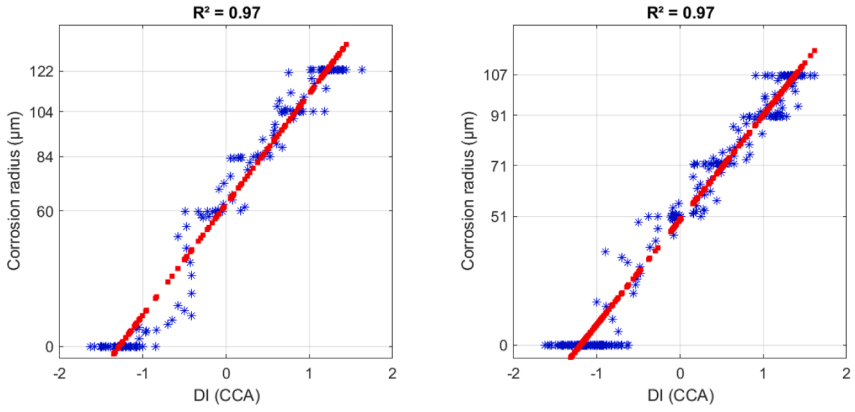

Experiment #1 *Experiment #2*

Fig. 12. Correlation between DI values after the dimension reduction step and corrosion pit radius for the first experiment [left] and the second experiment [right].

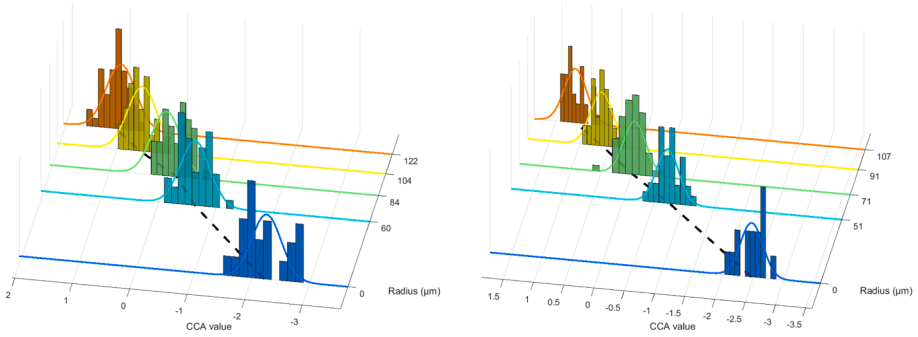

Fig. 13. DIs distribution with associated Gaussian models for the first [left] and second [right] experiments.

And then for a given corrosion pit damage of size R, the POD associated with the DI threshold T can be computed as Eq. (6).

$$POD(T,R) = \int_{T}^{+\infty} p_D(DI,R)dDI = \int_{T}^{+\infty} p(DI|r=R)dDI \tag{6}$$

It follows that given a selected PFA, the threshold T that needs to be selected to ensure it can be computed by inverting Eq. (5). Then, given a POD to obtain and the previously computed threshold T, the minimum radius R allowing to achieve it under the previously specified PFA can be computed by inverting Eq. (6).

In Fig. 14, the minimum detectable radius r under a given PFA and a given POD according to data collected in the first experiment [left] of the second experiment [right] is shown for various PFA ranging from 1 % to 10 % and for various POD ranging from 90 % to 98 %. From these figures, it can be shown that, as expected, when the PFA is increasing (*i.e.* when more false alarms are accepted) or when the POD is decreasing (*i.e.* when a lower detection rate is tolerated), the minimum detectable radius is decreasing. As a good order of magnitude representative of the proposed method ability to resolve a given corrosion pit damage, a PFA of 5 % associated with a POD of 95 % can be retained. For those values, a minimum radius $r \simeq 30$ µm can be detected for the first experiment and a minimum radius $r \simeq 20$ µm can be detected for the second. For detection purposes, the method is thus rather satisfying from an industrial point of view as it merely corresponds to what can be detected visually by an experienced operator, but automatically.

4.2. Damage localization

Once the presence of corrosion pit damage has been assessed, the upcoming SHM step consists in localizing the damage on the structure to be monitored. In order to achieve this goal, the measured LW signals are directly used to feed a given damage localization algorithm without the need of DI computation and dimension reduction steps. The algorithm being used here relies on a tensorial decomposition of the acquired LW signals [55]. A tensor, from a signal processing point of view, can be seen as a matrix having more than two dimensions. Indeed, when interrogating such a structure using Lamb waves, the resulting data lie along three dimensions (namely the *"actuator"*, *"sensor"*, and *"time"* dimensions) and can thus be interpreted as three-way tensors. The canonical polyadic decomposition of a tensor is a mathematical expression using one simpler dimensional vectors that allows to unveil the underlying tensor structure. Under classical assumptions regarding wave propagation, the canonical polyadic decomposition of rank 2 of the tensors build from the phase and amplitude of the difference signals between a healthy and damaged states provides direct estimates of the distances between the piezoelectric elements and damage. This useful property has been used to compute damage localization maps on the basis of these estimates. As a summary, this approach proposes an tensor-based damage localization algorithm that has previously successfully validated on experimental data coming from a scale one part of an airplane [55]. The details of the algorithms will not be presented here and only corrosion pit localization results computed on the basis of LW signals acquired during both experiments will be presented in order to demonstrate the completeness of the proposed approach in terms of SHM. The interested readers can still refer to the original publication [55] to get a full understanding of the technical points.

A summary of the damage localization results provided for the first and second experiments by the tensor-based localization algorithm is shown in Fig. 15 [left] and a typical localization result corresponding to the first experiment with a corrosion pit size of 60 µm is shown in Fig. 15 [right]. Those results demonstrate that with the LW signals acquired here in situ, µm-sized corrosion pits localization is achieved with a precision of $\simeq 6-7$ mm given a plate of dimension 8 cm by 12.5 cm. In terms of accuracy, the localization error is here around 6 % with respect to the plate dimensions. This results is in good agreement with the damage localization accuracy of the tensor-based damage localization algorithm. Such a localization accuracy is also acceptable in practice from an industrial point of view as it will allows to efficiently guide a

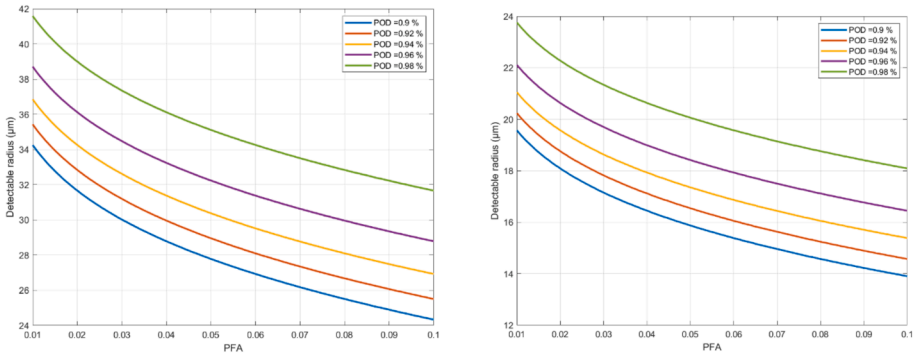

Fig. 14. Minimum detectable radius under a given PFA and a given POD according to data collected in the first experiment [left] of the second experiment [right].

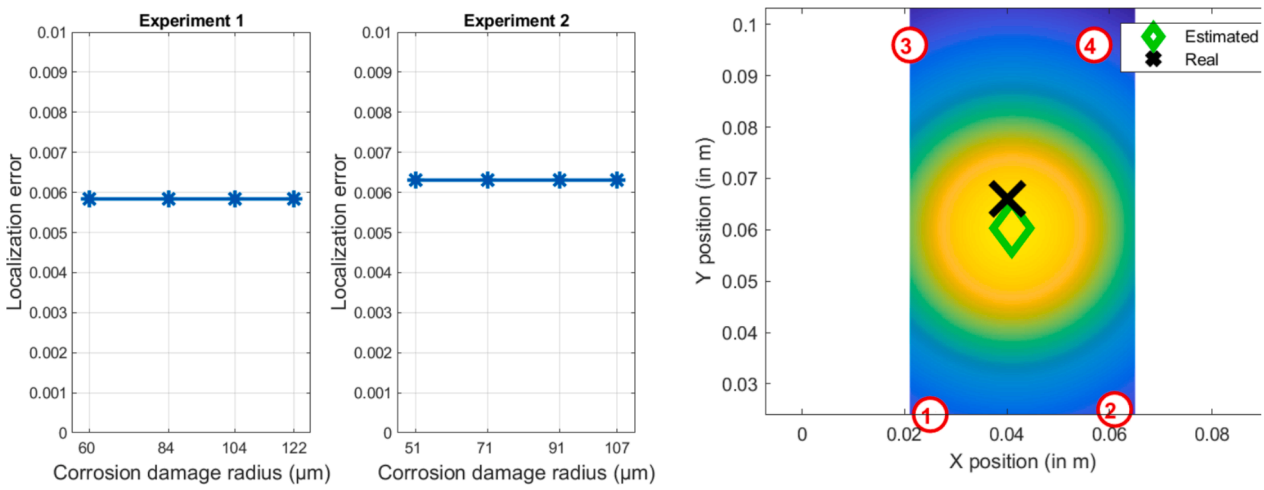

Fig. 15. Damage localization results summary for the first and second experiments [left] and typical localization result (first experiment, corrosion pit size of radius 60 μm) [right].

maintenance operator toward a specific area to be visually inspected and fixed if necessary. In terms of resolution, it can be chosen by the user and here a resolution of 0.4 mm in the x-direction and of 0.625 mm in the y-direction have been achieved. In summary, it can be concluded that the μm-sized corrosion pit can be accurately enough localized in the present case.

4.3. Damage size extrapolation

Finally, the last step of the SHM process investigated here consists in being able to quantify corrosion pits size given only the measured LW signals or equivalently the DIs after the reduction dimension steps. What is more precisely targeted here is to achieve corrosion pits size extrapolation, *i.e.* to be able to predict upcoming larger corrosion pit damage size on the basis of information acquired only on smaller corrosion pits. It is a two steps extrapolation process. As a first step, a linear model relating the corrosion pit radius to the reduced dimension DI is being learnt. This linear model is learnt only from small damage radii. Then, during the extrapolation step, DIs are computed for signals measured with larger values of corrosion radii. Finally, by inverting the linear model relating the DI value with the corrosion pit radii, it is then possible to infer the actual damage radii from the reduced dimension DI and thus to predict it. More details regarding those steps are provided in the following.

In practice, according to the linear correlation demonstrated between the reduced dimension DI and the corrosion pit radius, a linear model relating the reduced dimension $DI(r)$ to the actual damage size r is first learnt only on small damages with radii lying between 0 and r_{min}:

$$DI(r) = \mu_0 + \alpha r, r \in [0, r_{min}] \tag{7}$$

The estimated corrosion pit damage size $\widehat{r}$ is then computed from $DI(r)$ by inverting the previously learnt linear model for larger corrosion pit radii lying between r_{min} and r_{max} as follows:

$$\widehat{r} = \frac{DI(r) - \mu_0}{\alpha}, r \in [r_{min}, r_{max}] \tag{8}$$

The only parameter in that corrosion pit size extrapolation method is related with the range of radii $[0, r_{min}]$ used for learning and can be set up as a percentage value of r_{max}. In order to filter out rapid estimation variations, estimated radii are averaged over 3 values (*i.e.* over 30 s) using a moving average algorithm. It should be noticed that performing extrapolation is particularly challenging and that classically damage quantification algorithms encountered in SHM only perform interpolation, *i.e.* damage size prediction inside the range where the learning phase has been achieved [56].

Results of corrosion pit radius extrapolation for the first and second experiments and for various learning rates of 70 %, 80 %, and 100 % are shown in Fig. 16 and Fig. 17. For the first experiment, it can be seen in Fig. 16 that whatever the selected learning rate, the learning is correctly achieved (*i.e.* the green dots are lying close to the blue line) but the extrapolation has a tendency to overestimate the actual corrosion pit radius. This tendency for overestimation however decreases when the learning rate is increasing. For the second experiment, it can be seen on Fig. 17 that learning is correctly achieved for all learning rates but that the tendency to overestimate is not observed here. However, the estimated radii are more widespread for the second experiment than for the first one. In conclusion, it can be stated that obtained results are always satisfying in the learning phase and that in the extrapolation phase results are satisfying for the second experiment but are overestimated for the first one. Nevertheless, such results remains acceptable in practice from an industrial perspective. In terms of maintenance, what is interesting here is to be able to learn DI evolution from small corrosion pit damages that do not impart safety, and from this learning to be able to issue a warning signal when the monitored damage crosses a predefined safety threshold.

5. Discussion

The previous section has demonstrated that the correlation found between the corrosion pit size and the reduced dimension space can be useful for SHM purposes as it allows to efficiently detect, localize and extrapolate the upcoming size of corrosion pit damages. However, some key points underlying the proposed approach are discussed here.

5.1. Wavelength versus corrosion pit radius

A first point to discuss is related to the physical properties of the LW being used here to monitor the apparition of corrosion pit damages. In the low frequency range, LW are multimodal and dispersive. This means in practice that for a given frequency, at least two different waves can propagate at different group velocities and that those group velocities are changing with the frequency. The two modes existing in the lower frequency range are the A_0 and S_0 modes corresponding to the flexural and longitudinal waves. The wavelengths and group velocities associated with the A_0 and S_0 modes for the steel coupons being monitored here have been computed [57,58] and are shown in Fig. 18. From this figure it can be seen that at 200 kHz, the S_0 mode travels with a group velocity of 5 km/s and with a wavelength of 25 mm whereas the A_0

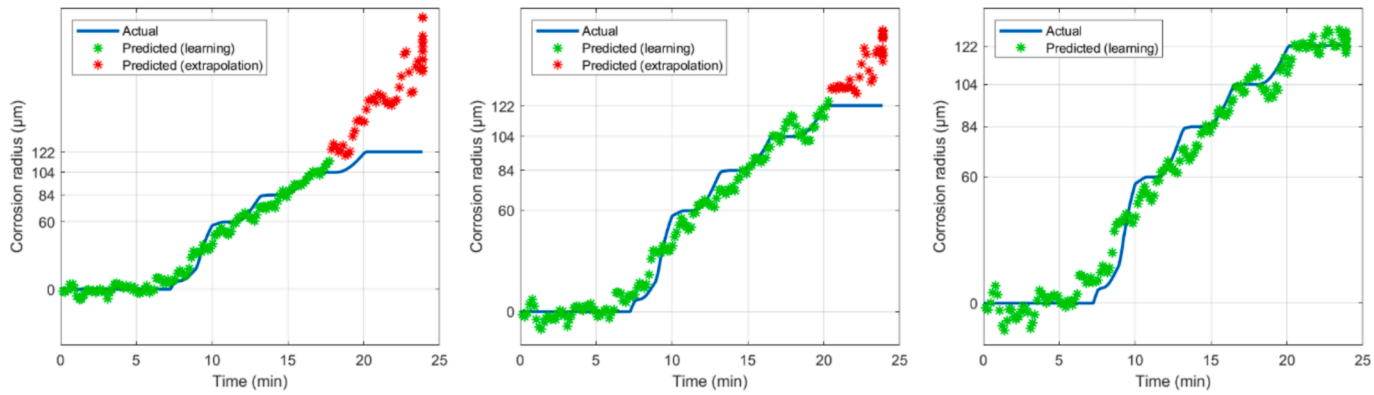

Fig. 16. Corrosion pit radius extrapolation for the first experiment and for various learning rates (70% [left], 80% [center] and 100% [right]).

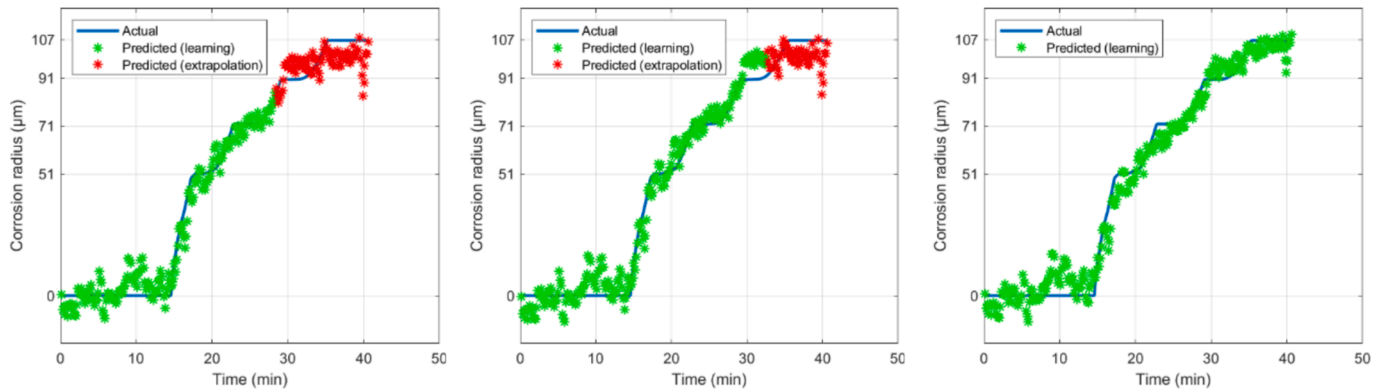

Fig. 17. Corrosion pit radius extrapolation for the second experiment and for various learning rates (70% [left], 80% [center] and 100% [right]).

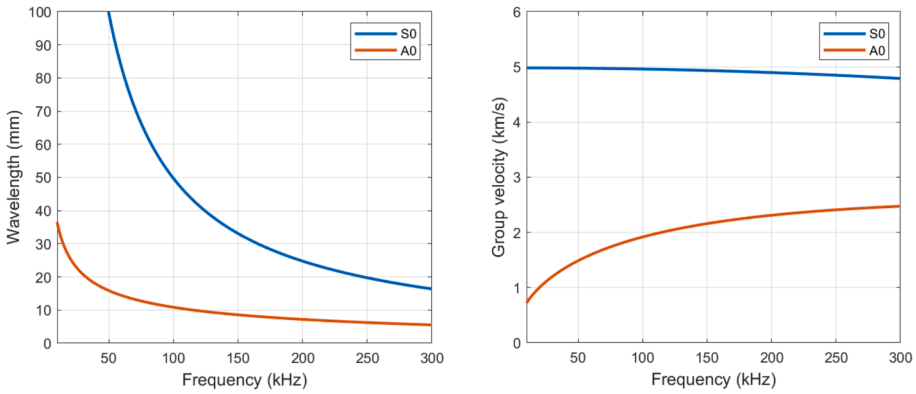

Fig. 18. Wavelength and group velocity as a function of frequency for the steel coupon.

mode travels with a group velocity of 2.3 km/s and with a wavelength of 8 mm. Furthermore, the previous computations also allow to conclude that both modes coexists at the selected frequency and that the A0 mode is slightly dominant.

A classical condition [47] for selecting the working frequency allowing to detect a damage having a given size d consists in choosing a frequency f such that the corresponding wavelength λ is smaller than $\frac{d}{2}$. This condition ensures that diffraction phenomenon will appear during the interaction between the incoming LW and the damage to be monitored. It has however been demonstrated in Section 4.1 that a $\simeq 30$ µm corrosion pit can be detected using LW having wavelengths of 25 mm for S_0 and of 8 mm for A_0. The results presented here are thus very far from the classical condition exposed before as the wavelength to damage size ratio is equal to $\simeq 260$ for A_0 and to $\simeq 800$ for S_0. The classical condition mentioned above is ensuring that large diffraction phenomenon will occur. However, this condition is not stating that nothing will occur for lower frequencies and thus for larger wavelengths. For such lower frequencies, reflection phenomenon can still occur, even if they are of small amplitude [59,60,61]. This is very likely what is observed here and what allows to perform corrosion pit monitoring.

5.2. *Effect of a bubble*

The second point that will be discussed here is related with the experimental protocol that has been proposed here for unique corrosion pit damage generation. This experimental protocol relies on a very thin capillary which drives the flow of corrosive liquid to the desired pit location. Unexpectedly, during the second experiment, a bubble having

a radius of $\simeq$ 500 μm appeared at the output of the capillary as some air has been accidentally trapped into it (see Fig. 19 [left]). This bubble has been manually evacuated a few minutes after its apparition. The data with the bubble have not been removed from the analysis performed in Sections 3 and 4 regarding the second experiment. The question arose if the proposed method is indeed able to monitor such a small bubble.

Fig. 19 is showing the corrosion pit size radii estimated using the FFT DI computed directly for the path going from the PZT actuator 1 to the PZT sensor 3 without dimension reduction steps. On this figure, it can be seen that the estimated radii closely follow the actual radii but not at the moments in time where the bubble occurred. This means that this specific DI is indeed sensitive to the presence of the bubble. However, such a drop in estimated radii is not observed in Fig. 17 whereas the bubble was still there. The reason for that is that radii presented in Fig. 17 are estimated from DI after the dimension reduction steps. The first dimension reduction step is a simple spatial integration, but the second dimension reduction step is CCA which looks for the linear combination of available DIs allowing to maximize the correlation with corrosion pit size. As the presence of the bubble was not expected, CCA has discarded from the linear combination all the DIs that were sensitive to the presence of the bubble in order to retain only the ones that were sensitive to the corrosion pit damage. Consequently, this explains why the bubble drop is not observed in Fig. 17. Finally, it can be said that the proposed method is indeed sensitive to the presence of bubbles. This could be very useful for corrosion monitoring as corrosion in aqueous liquid can produce H_2 bubbles near the corrosion location.

5.3. Transfer learning opportunities

A last point to discuss is related with transfer learning. An interesting idea would be to be able to learn DI evolution on one experiment and then to be able to transfer this knowledge to another experiment. As here, two independent experiments are available, such an approach can be studied. However, both experiments are not perfect. Indeed, corrosion radii predictions appeared to be a bit overestimated in the first experiment (see Fig. 16) and the second experiment suffered from the apparition of a undesirable bubble (see Section 5.2). In order to get clean learning data, data from the second experiment but without the ones corresponding to the bubble have been selected for learning purposes. The results of the learning phase on such data are shown in Fig. 20 [Left] and it can be seen that the estimated radii are following extremely closely the actual ones, much more closely than when learning with the bubble data (see Fig. 17). From those data, two things are learned: the dimension reduction step allowing to compute the optimal combination of DIs and the linear model relating the CCA DI to the actual corrosion pit radius.

On Fig. 20 [Center], the reduction dimension step and the model learnt from the second experiment without bubble are applied to the first experiment. It appears that the predicted radii follows the actual ones in terms or order of magnitude. The fit is not perfect but sufficiently convincing to conclude that the model that has been learnt caught some relevant physical information. And consistently with Fig. 16, an overestimation is observed for the last radii predictions. On Fig. 20 [Right], the reduction dimension step and the model learnt from the second experiment without bubble are finally applied to the second experiment data but including the bubble. Out of the bubble region, performances similar to the one achieved in Fig. 20 [left], are observed which was to be expected. However, inside the bubbe region, it can be seen that the effect of the bubble can still be clearly observed. So, as the bubble data were no present during the learning process, the effect of the bubble has not been filtered out by the CCA dimension reduction step as it was the case in Fig. 17.

5.4. Influence of bonding adhesive and of temperature

The adhesives being used here are adhesives that are qualified for aeronautic applications. Consequently, they are designed to handle temperature ranges and humidity conditions that are practically encountered in aeronautic applications. Additionally, the four PZT being used to send and receive Lamb waves are covered by a protective layer in order to avoid electrical or chemical interactions with the solution. It is thus very unlikely that the adhesive will degrade or that the PZT will debond from the host structure in the present experiments. For practical deployment of such a corrosion monitoring solution, PZT debonding or damaging can however easily be controlled using impedance measurements [62].

The temperature may also have an important effect on Lamb waves propagation in the structure [63]. It will practically slightly change the group velocity and the attenuation in the material thus leading to amplitude decrease and phase shift. However here, care has been taken here to control the temperature of the experimental setup and of its environment. Experiments were carried out in a temperature controlled environment and all the solutions were stored in the same controlled environment room, thus ensuring that their temperature is also controlled. Consequently, no effect of temperature should be observed in this experimental campaign. For practical deployment of such a corrosion monitoring solution, temperature compensation strategies dedicated to Lamb waves can however be considered [63].

6. Conclusion

Corrosion is a major threat in the aeronautic industry, both in terms of safety and cost. Efficient, versatile, and cost affordable solutions for corrosion monitoring are thus needed. Ultrasonic Lamb Waves (LW)

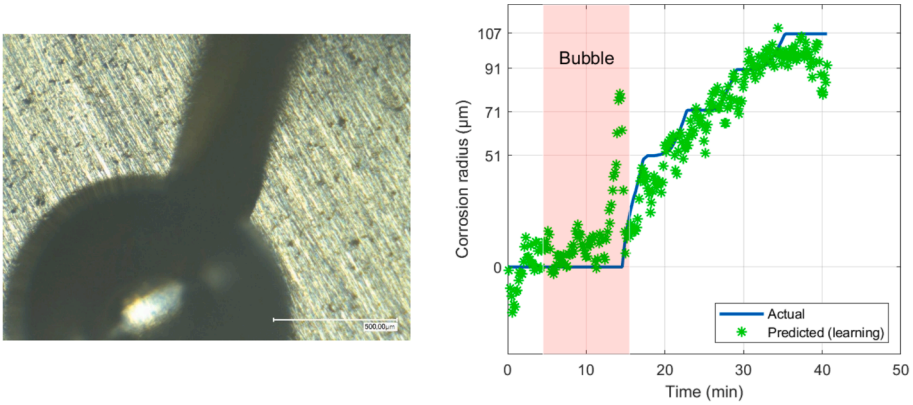

Fig. 19. [Left] Picture of the bubble appeared during the second experiment and [Right] the effect of the bubble on the radii estimations performed using FFT DI for the path going from the PZT actuator 1 to the PZT sensor 3 without dimension reduction steps.

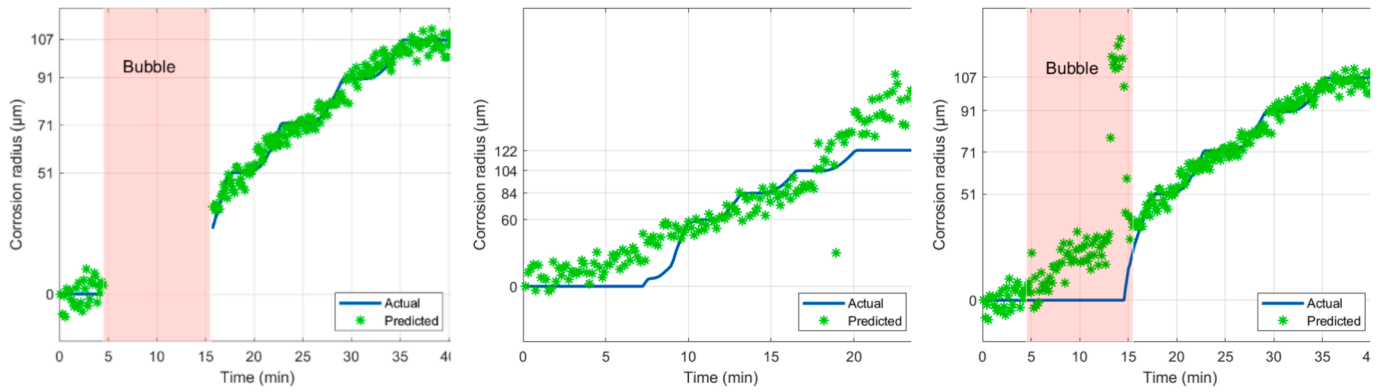

Fig. 20. Transfer learning between experiments. [Left] Learning on experiment 2, without data with bubble. [Center] Prediction on experiment 1. [Right] Prediction on experiment 2 with all data.

appear as very efficient for corrosion monitoring and can be made cost effective and versatile if emitted and received by a sparse array of piezoelectric elements (PZT). A LW solution relying on a sparse PZT array and allowing to monitor µm-sized corrosion pit growth on stainless 316L grade steel plate is here evaluated. Experimentally, the corrosion pit size is electrochemically controlled by both the imposed electrical potential and the injection of a corrosive NaCl solution through a capillary located at the desired pit location. In parallel, the corrosion pit growth is monitored in-situ every 10 s by sending and measuring LW using a sparse array of 4 PZTs bonded to the back of the steel plate enduring corrosion. As a ground truth information, the corrosion pit volume is estimated as the dissolved volume balancing the electronic charges exchanged during corrosion. The corrosion pit radius is additionally checked post-experiment precisely with an optical measurement. Measured LW signals are then post-processed in order to compute a collection of synthetic damage indexes (DIs). After dimension reduction steps, obtained DI values correlates extremely well with the corrosion pit radius. Using a linear model relating those DI values to corrosion pit radius, it is demonstrated that corrosion pit from 30 µm to 150 µm can be reliably detected, located with a precision of 5–6 mm, and their upcoming size extrapolated. Two independent experiments were achieved in order to ensure the repeatability of the proposed approach and data are available in Open Access [64]. LW managed by a sparse PZT array thus appears to be reliable and efficient to monitor growth of µm-sized corrosion pits on 316L steel plates. If embedded in aeronautical structure, such an approach could be a versatile and cost-effective alternative to actual non-destructive maintenance procedures that are both time and manpower consuming.

CRediT authorship contribution statement

C. Nicard: Writing – original draft, Investigation, Data curation. **M. Rébillat:** Software, Methodology, Investigation, Funding acquisition. **O. Devos:** Writing – original draft, Validation, Supervision, Methodology. **M. El May:** Validation, Supervision, Methodology, Investigation. **F. Letellier:** Validation, Software. **S. Dubent:** Methodology, Investigation, Data curation. **M. Thomachot:** Software, Project administration. **M. Fournier:** Validation, Software. **P. Masse:** Methodology, Investigation. **N. Mechbal:** Writing – review & editing, Funding acquisition, Conceptualization.

Declaration of competing interest

The authors declare the following financial interests/personal relationships which may be considered as potential competing interests: [REBILLAT Marc reports financial support was provided by French National Research Agency. If there are other authors, they declare that they have no known competing financial interests or personal relationships that could have appeared to influence the work reported in this paper.].

Acknowledgement

The author would like to thank the French “Agence Nationale de la Recherche” (ANR) for the funding of the COQTEL project under the grant number ANR-20-CE42-0014 that allowed to produce the results presented in this manuscript.

Appendix

Table A1
Mathematical definitions of the damage indexes (DIs).

DI name	Comments	Definition
CC	FFT based implementation of the maximum of the correlation	$1-\max\left(\frac{IFFT\left[FFT\left[x_{ij(t)}\right]\times FFT\left[y_{ij}(t)\right]^{*}\right]}{\sqrt{\left(E_{x_{ij}}\times E_{y_{ij}}\right)}}\right)$
CCA	MATLAB based implementation of the maximum of the correlation	$1-\max\left(xcorr\left[x_{ij}(t),y_{ij}(t)\right]\right)$
CC0	MATLAB based implementation of the zero-lag correlation	$1-xcorr\left[x_{ij}(t),y_{ij}(t)\right](0)$
CRC	MATLAB-based implementation of the correlation coefficient	$1-corrcoeff\left[x_{ij}(t),y_{ij}(t)\right]$
MEAN	Mean of the difference signal	$\frac{1}{T}\int_0^T\left(x_{ij}(t)-y_{ij}(t)\right)dt$

(*continued on next page*)

Table A1 (*continued*)

DI name	Comments	Definition
MEANABS	Mean of the absolute value of the difference signal	$\frac{1}{T}\int_0^T \left\| x_{ij}(t) - y_{ij}(t) \right\| dt$
STD	Standard deviation of the difference signal	$\sqrt{\frac{1}{T}\int_0^T \left(x_{ij}(t) - y_{ij}(t) \right)^2 dt}$
STDABS	Standard deviation of the absolute value of the difference signal	$\sqrt{\frac{1}{T}\int_0^T \left\| x_{ij}(t) - y_{ij}(t) \right\|^2 dt}$
SKW	Skewness of the difference signal	$\left[\frac{1}{T}\int_0^T \left(x_{ij}(t) - y_{ij}(t) \right)^3 dt\right]^{\frac{1}{3}}$
SKWABS	Skewness of the absolute value of the difference signal	$\left[\frac{1}{T}\int_0^T \left\| x_{ij}(t) - y_{ij}(t) \right\|^3 dt\right]^{\frac{1}{3}}$
KUR	Kurtosis of the difference signal	$\left[\frac{1}{T}\int_0^T \left(x_{ij}(t) - y_{ij}(t) \right)^4 dt\right]^{\frac{1}{4}}$
KURABS	Kurtosis of the absolute value of the difference signal	$\left[\frac{1}{T}\int_0^T \left\| x_{ij}(t) - y_{ij}(t) \right\|^4 dt\right]^{\frac{1}{4}}$
NRE	Normalized residual energy	$\frac{\int_0^T \left(x_{ij}(t) - y_{ij}(t) \right)^2 dt}{2 \times \left(\int_0^T x_{ij}(t)^2 dt + \int_0^T y_{ij}(t)^2 dt \right)}$
NRE2	Normalized residual energy 2	$\frac{\int_0^T x_{ij}(t)^2 dt - \int_0^T y_{ij}(t)^2 dt}{max\left(\int_0^T x_{ij}(t)^2 dt, \int_0^T y_{ij}(t)^2 dt \right)}$
NRE3	Normalized residual energy 3	$1 - \frac{min\left(\int_0^T x_{ij}(t)^2 dt, \int_0^T y_{ij}(t)^2 dt \right)}{max\left(\int_0^T x_{ij}(t)^2 dt, \int_0^T y_{ij}(t)^2 dt \right)}$
NRE4	Normalized residual energy 4	$\sqrt{\frac{\int_0^T \left(x_{ij}(t) \times y_{ij}(t) \right)^2 dt}{\int_0^T x_{ij}(t)^2 dt \times \int_0^T y_{ij}(t)^2 dt}}$
NRE5	Normalized residual energy 5	$\frac{\int_0^T \left(\frac{x_{ij}(t)}{\max(x_{ij})} - \frac{y_{ij}(t)}{\max\left(y_{ij}\right)} \right)^2 dt}{2 \times \left(\int_0^T [x_{ij}(t)/\max(x_{ij})]^2 dt + \int_0^T [y_{ij}(t)/\max\left(y_{ij}\right)]^2 dt \right)}$
NRE6	Normalized residual energy 6	$(1 - NRE4) \times \frac{min\left(\int_0^T x_{ij}(t)^2 dt, \int_0^T y_{ij}(t)^2 dt \right)}{max\left(\int_0^T x_{ij}(t)^2 dt, \int_0^T y_{ij}(t)^2 dt \right)}$
MA	Maximum amplitude of the difference	$\max\left[x_{ij}(t) - y_{ij}(t) \right]$
MAR	Maximum Amplitude Relative	$\frac{\max\left(\left\| x_{ij}(t) - y_{ij}(t) \right\| \right)}{\max\left(\left\| x_{ij}(t) \right\| \right)}$
FFT	FFT ratio of the difference signal over the sum of signals at f_0	$\frac{FFT\left[x_{ij}(t) - y_{ij}(t) \right]_{f=f_0}}{FFT\left[x_{ij}(t) + y_{ij}(t) \right]_{f=f_0}}$
NL_HARM2	FFT ratio of the difference signal at $2f_0$ over f_0	$\frac{FFT\left[x_{ij}(t) - y_{ij}(t) \right]_{f=2f_0}}{FFT\left[x_{ij}(t) - y_{ij}(t) \right]_{f=f_0}}$
NL_HARM3	FFT ratio of the difference signal at $3f_0$ over f_0	$\frac{FFT\left[x_{ij}(t) - y_{ij}(t) \right]_{f=3f_0}}{FFT\left[x_{ij}(t) - y_{ij}(t) \right]_{f=f_0}}$
NL_HARM4	FFT ratio of the difference signal at $4f_0$ over f_0	$\frac{FFT\left[x_{ij}(t) - y_{ij}(t) \right]_{f=4f_0}}{FFT\left[x_{ij}(t) - y_{ij}(t) \right]_{f=f_0}}$
NL_HARM5	FFT ratio of the difference signal at $5f_0$ over f_0	$\frac{FFT\left[x_{ij}(t) - y_{ij}(t) \right]_{f=5f_0}}{FFT\left[x_{ij}(t) - y_{ij}(t) \right]_{f=f_0}}$
NL_THD	Total harmonic distortion of the difference signal	$D(f) = FFT\left[x_{ij}(t) - y_{ij}(t) \right],\ THD = \sum_{n=2}^{5} \frac{D(nf_0)^2}{D(f_0)^2}$
NL_SPEC	Sprectral energy in the "nonlinear" part versus the "linear" one	$D(f) = FFT\left[x_{ij}(t) - y_{ij}(t) \right],\quad S = \sqrt{\frac{\int_{1.3f_0}^{5f_0} D(f)^2 df}{\int_0^{1.3f_0} D(f)^2 df}}$
ENV	Energy of the envelope of the difference	$\sqrt{\frac{\sum_{t=T_1}^{T_2} env\left[y_{ij}(t) - x_{ij}(t) \right]^2}{\sum_{t=T_1}^{T_2} env\left[x_{ij}(t) \right]^2}}$

(*continued on next page*)

Table A1 (*continued*)

DI name	Comments	Definition
PHI	Energy of the phase of the difference	$\sqrt{\frac{\sum_{t=T_1}^{T_2}\Phi\left[y_{ij}(t)-x_{ij}(t)\right]^2}{\sum_{t=T_1}^{T_2}\Phi\left[x_{ij}(t)\right]^2}}$
TDM	Time Delay of Max	$\frac{\mathrm{argmax}(\mathscr{H}\left(y_{ij}(t)\right)-\mathrm{argmax}(\mathscr{H}\left(x_{ij}(t)\right)}{\mathrm{argmax}\left(\mathscr{H}\left(x_{ij}(t)\right)\right)}$
TD1	Time Delay of the first wave packet	$TD1 = \frac{t_2-t_1}{t_1}$
SAPR	Signal Amplitude Peak Ratio	$\left\lvert 1-\frac{\max\left(\left\lvert y_{ij(t)}\right\rvert\right)}{\max\left(\left\lvert x_{ij(t)}\right\rvert\right)}\right\rvert$
SAPS	Signal Amplitude Peak Squared percentage differences	$\left[\frac{\max\left(\left\lvert y_{ij(t)}\right\rvert\right)-\max\left(\left\lvert x_{ij(t)}\right\rvert\right)}{\max\left(\left\lvert x_{ij(t)}\right\rvert\right)}\right]^2$
SAHM	Signal Amplitude Hilbert transform Maximum	$\left[\frac{\max\left(\left\lvert\mathscr{H}(y_{ij}(t))\right\rvert\right)-\max\left(\left\lvert\mathscr{H}(x_{ij}(t))\right\rvert\right)}{\max\left(\left\lvert\mathscr{H}(y_{ij}(t))\right\rvert\right)}\right]^2$
SSSD	Signal Sum of Squared Differences	$\frac{\int_0^T\left(x_{ij}(t)-y_{ij}(t)\right)^2dt}{\int_0^T x_{ij}(t)^2dt}$
CCTOF	Cross-correlation-based TOF percentage difference	$\left\lvert\frac{\mathrm{argmax}\left(xcorr\left[x_{ij}(t),x_{ij}(t)\right]\right)-\mathrm{argmax}\left(xcorr\left[x_{ij}(t),y_{ij}(t)\right]\right)}{\mathrm{argmax}\left(xcorr\left[x_{ij}(t),x_{ij}(t)\right]\right)}\right\rvert$
WPSD	Welch-based Power Spectral Density	–
WTF	Welch-based transfer function	–
CCMPD	Cross-correlation maximum percentage difference	–
DWTC	Discrete Wavelet Transform approximation coefficients	–

Data availability

Data are available in Open Access at 10.5281/zenodo.14193335

References

[1] S. Benavides, Corrosion control in the aerospace industry, Elsevier, 2009.
[2] S.J. Harris, M. Mishon, M. Hebbron, Corrosion sensors to reduce aircraft maintenance. In Workshop on Enhanced Aircraft Platform Availability through Advanced Maintenance Concepts and Technologies, 2006.
[3] M.S.B. Reddy, D. Ponnamma, K.K. Sadasivuni, S. Aich, S. Kailasa, H. Parangusan, M. Ibrahim, S. Eldeib, O. Shehata, M. Ismail, et al., Sensors in advancing the capabilities of corrosion detection: A review, Sens. Actuators, A 332 (2021) 113086.
[4] V. Vasagar, M. K. Hassan, A. M. Abdullah, A. V. Karre, B. Chen, K. Kim, N. Al-Qahtani, T. Cai et al., Non-destructive techniques for corrosion detection: A review, Corros. Eng. Sci. Technol. p. 1478422X241229621, 2024.
[5] V. S. Agarwala, P. L. Reed, S. Ahmad et al., Corrosion detection and monitoring-A review,» NACE CORROSION, p. NACE–00271, 2000.
[6] D. Balageas, C.-P. Fritzen, A. Güemes et al., Structural health monitoring, vol. 493, Wiley Online Library, (2006).
[7] C.R. Farrar, K. Worden, et al., An introduction to structural health monitoring, Philosophical Transactions of the Royal Society of London A: Mathematical Phys. Eng. Sci. 365 (2007) 303–315.
[8] K. Worden, C. R. Farrar, G. Manson et G. Park, «The fundamental axioms of structural health monitoring,» Proceedings of the Royal Society of London A: Mathematical, Physical and Engineering Sciences, vol. 463, pp. 1639-1664, 2007.
[9] C. Jirarungsatian, A. Prateepasen, Pitting and uniform corrosion source recognition using acoustic emission parameters, Corros. Sci. 52 (2010) 187–197.
[10] P. Kudela, M. Radzienski, W. Ostachowicz, Z. Yang, Structural Health Monitoring system based on a concept of Lamb wave focusing by the piezoelectric array, Mech. Syst. Sig. Process. 108 (2018) 21–32.
[11] S. Grondel, C. Delebarre, J. Assaad, J.-P. Dupuis, L. Reithler, Fatigue crack monitoring of riveted aluminium strap joints by Lamb wave analysis and acoustic emission measurement techniques, Ndt & E International 35 (2002) 137–146.
[12] F. Zou, F. Cegla, et al., High accuracy ultrasonic corrosion monitoring, Chez NACE CORROSION (2017).
[13] U.C. Thibbotuwa, A. Cortés, A. Irizar, et al., Small ultrasound-based corrosion sensor for intraday corrosion rate estimation, Sensors 22 (2022) 8451.
[14] M. Farin, E. Moulin, L. Chehami, F. Benmeddour, C. Nicard, P. Campistron, O. Bréhault, L. Dupont, et al., Monitoring saltwater corrosion of steel using ultrasonic coda wave interferometry with temperature control, Ultrasonics 124 (2022) 106753.
[15] C. Nicard, M. Farin, E. Moulin, D. Balloy, P. Serre, et al., Monitoring of generalised corrosion: Ultrasonic coda wave interferometry technique applied to steel corrosion in aqueous NaCl solutions, Mater. Chem. Phys. 305 (2023) 127908.
[16] W. Li, T. Liu, S. Gao, M. Luo, J. Wang, J. Wu, et al., An electromechanical impedance-instrumented corrosion-measuring probe, J. Intell. Mater. Syst. Struct. 30 (2019) 2135–2146.
[17] W. Li, T. Liu, D. Zou, J. Wang, T.-H. Yi, et al., PZT based smart corrosion coupon using electromechanical impedance, Mech. Syst. Sign. Process. 129 (2019) 455–469.
[18] Q. Bao, S. Yuan, F. Guo, L. Qiu, et al., Transmitter beamforming and weighted image fusion–based multiple signal classification algorithm for corrosion monitoring, Struct. Health Monit. 18 (2019) 621–634.
[19] M. Chang, S. Yuan, F. Guo, et al., Corrosion monitoring using a new compressed sensing-based tomographic method, Ultrasonics 101 (2020) 105988.
[20] R. Gorgin, Z. Wu, D. Gao, Y. Wang et al., Damage size characterization algorithm for active structural health monitoring using the A0 mode of Lamb waves, Smart Mater. Struct. vol. 23, p. 035015, 2014.
[21] J. Hua, X. Cao, Y. Yi, J. Lin, et al., Time-frequency damage index of Broadband Lamb wave for corrosion inspection, J. Sound Vib. 464 (2020) 114985.
[22] L. Huang, Z. Luo, L. Zeng, J. Lin, et al., Detection and localization of corrosion using the combination information of multiple Lamb wave modes, Ultrasonics 138 (2024) 107246.
[23] Z. Luo, L. Zeng, J. Lin, et al., A hidden corrosion detection method based on robust multimodal Lamb waves, Meas. Sci. Technol. 31 (2020) 044002.
[24] J. Rao, M. Ratassepp, D. Lisevych, M. Hamzah Caffoor, Z. Fan, et al., On-line corrosion monitoring of plate structures based on guided wave tomography using piezoelectric sensors, Sensors 17 (2017) 2882.
[25] D. Wang, W. Zhang, X. Wang, B. Sun, et al., Lamb-wave-based tomographic imaging techniques for hole-edge corrosion monitoring in plate structures, Materials 9 (2016) 916.
[26] X. Wang, M. Lin, J. Li, J. Tong, X. Huang, L. Liang, Z. Fan, Y. Liu, et al., Ultrasonic guided wave imaging with deep learning: Applications in corrosion mapping, Mech. Syst. Sig. Process. 169 (2022) 108761.
[27] L. Zeng, Z. Luo, J. Lin, J. Hua, et al., Excitation of Lamb waves over a large frequency-thickness product range for corrosion detection, Smart Mater. Struct. 26 (2017) 095012.
[28] X. Ding, C. Xu, M. Deng, Y. Zhao, X. Bi, N. Hu, et al., Experimental investigation of the surface corrosion damage in plates based on nonlinear Lamb wave methods, Ndt & E International 121 (2021) 102466.
[29] F. Jenot, M. Ouaftouh, M. Duquennoy, M. Ourak, et al., Corrosion thickness gauging in plates using Lamb wave group velocity measurements, Meas. Sci. Technol. 12 (2001) 1287.
[30] I. Ozolinsh, I. Pavelko, V. Pavelko, M. Wevers et H. Pfeiffer, «Some results of ultrasonic detection of uniform corrosion in thin Al2024-T3 sheets,» chez EU Project Meeting on Aircraft Integrated Structural Health Assessment (AISHA), Leuven, Belgium, 2007.

[31] V.T. Rathod, D.R. Mahapatra, et al., Ultrasonic Lamb wave based monitoring of corrosion type of damage in plate using a circular array of piezoelectric transducers, Ndt & E International 44 (2011) 628–636.
[32] A. Sedaghati, F. Honarvar, A.N. Sinclair, et al., Lamb wave-based experimental and numerical studies for detection and sizing of corrosion damage in metallic plates, Proceedings of the Institution of Mechanical Engineers, Part c: Journal of Mechanical Engineering Science 233 (2019) 2107–2120.
[33] B. Yoo, A. Purekar, et al., Corrosion damage monitoring using guided Lamb waves, chez Smart Mater. Adapt. Struct. Intell. Syst. (2012).
[34] L. Yu, V. Giurgiutiu, J. Wang, Y.-J. Shin, et al., Corrosion detection with piezoelectric wafer active sensors using pitch-catch waves and cross-time–frequency analysis, Struct. Health Monit. 11 (2012) 83–93.
[35] B. Zima, E. Roch, J. Moll, et al., Nondestructive corrosion degradation assessment based on asymmetry of guided wave propagation field, Ultrasonics 138 (2024) 107243.
[36] E.D. Parsons, H.H. Cudd, H.L. Lochte, et al., Synthetic corrosion pits and the analysis of their contents, J. Phys. Chem. 45 (1941) 1339–1345.
[37] P. Ernst, R.C. Newman, et al., Pit growth studies in stainless steel foils. I. Introduction and pit growth kinetics, Corros. Sci. 44 (2002) 927–941.
[38] K. Fushimi, K. Azumi, M. Seo, et al., Use of a liquid-phase ion gun for local breakdown of the passive film on iron, J. Electrochem. Soc. 147 (2000) 552.
[39] S.M. Ghahari, A.J. Davenport, T. Rayment, T. Suter, J.-P. Tinnes, C. Padovani, J. A. Hammons, M. Stampanoni, F. Marone, R. Mokso, et al., In situ synchrotron X-ray micro-tomography study of pitting corrosion in stainless steel, Corros. Sci. 53 (2011) 2684–2687.
[40] R.C. Alkire, K.P. Wong, et al., The corrosion of single pits on stainless steel in acidic chloride solution, Corros. Sci. 28 (1988) 411–421.
[41] S. Heurtault, R. Robin, F. Rouillard, V. Vivier, et al., On the propagation of open and covered pit in 316L stainless steel, Electrochim. Acta 203 (2016) 316–325.
[42] G. Jaussaud, J. Rebufa, M. Fournier, M. Logeais, N. Bencheikh, M. Rébillat, M. Guskov, et al., Improving Lamb Wave detection for SHM using a dedicated LWDS electronics. Chez 11th Symposium on NDT in Aerospace, 2019.
[43] M. Rebillat, M. Fournier, M. Thomachot, J. Rebufa, et al., Conception d'un système de SHM fonctionnant en modes actif et passif, chez 16ème Congrès Français d'Acoustique, CFA2022, Marseille, (2022).
[44] J. Rebufa, G. Jaussaud, M. Fournier, M. Logeais, N. Bencheikh, F. Claeyssen, M. Rébillat, M. Guskov, et al., Improving efficiency and robustness of structural health monitoring techniques based on lamb wave detection, (2019).
[45] Z. Su, Ye, et al. Identification of damage using Lamb waves: from fundamentals to applications, vol. 48, Springer Science & Business Media, 2009.
[46] C. Fendzi, N. Mechbal, M. Rebillat, M. Guskov, G. Coffignal, et al., A general Bayesian framework for ellipse-based and hyperbola-based damage localization in anisotropic composite plates, J. Intell. Mater. Syst. Struct. 27 (2016) 350–374.
[47] E. Lize, M. Rebillat, N. Mechbal, C. Bolzmacher, et al., Optimal dual-PZT sizing and network design for baseline-free SHM of complex anisotropic composite structures, Smart Mater. Struct. (2018).
[48] A. Rahbari, M. Rébillat, N. Mechbal, S. Canu, et al., Unsupervised damage clustering in complex aeronautical composite structures monitored by Lamb waves: An inductive approach, Eng. Appl. Artif. Intel. 97 (2021) 104099.
[49] R. Hajrya, N. Mechbal, et al., Principal component analysis and perturbation theory based robust damage detection of multifunctional aircraft structure, Struct. Health Monitor. Int. J. 12 (2013) 263–277.
[50] M. Barker, W. Rayens, et al., Partial least squares for discrimination, J. Chemometr. J. Chemometr. Soc. 17 (2003) 166–173.
[51] Rosipal, L. J. Trejo, B. Matthews, et al., «Kernel PLS-SVC for linear and nonlinear classification,» chez Proceedings of the 20th International Conference on Machine Learning (ICML-03), 2003.
[52] R. Rosipal, N. Krämer et al. «Overview and recent advances in partial least squares,» chez International Statistical and Optimization Perspectives Workshop" Subspace, Latent Structure and Feature Selection", 2005.
[53] J. Arenas-Garcia, K.B. Petersen, G. Camps-Valls, L.K. Hansen, et al., Kernel multivariate analysis framework for supervised subspace learning: A tutorial on linear and kernel multivariate methods, IEEE Signal Process Mag. 30 (2013) 16–29.
[54] M. Rebillat, O. Hmad, F. Kadri, N. Mechbal, et al., Peaks Over Threshold–based detector design for structural health monitoring: Application to aerospace structures, Struct. Health Monit. 17 (2018) 91–107.
[55] M. Rebillat, N. Mechbal, et al., Damage localization in geometrically complex aeronautic structures using canonical polyadic decomposition of Lamb wave difference signal tensors, Struct. Health Monit. 19 (2020) 305–321.
[56] W. Briand, Lamb waves based active sparse tomography for damage size quantification in composite structures: data-driven and parameter inversion methods, (2022).
[57] S. Guo, M. Rébillat, N. Mechbal, et al., Dichotomy property of dispersion equation of guided waves propagating in anisotropic composite plates, Mech. Syst. Signal Process. 164 (2022).
[58] S. Guo, M. Rébillat, N. Mechbal, et al., Prediction of frequency and spatially dependent attenuation of guided waves propagating in mounted and unmounted A380 parts made up of anisotropic viscoelastic composite laminates, Struct. Health Monitor. (2022).
[59] O. Diligent, T. Grahn, A. Boström, P. Cawley, M.J.S. Lowe, et al., The low-frequency reflection and scattering of the S 0 Lamb mode from a circular through-thickness hole in a plate: finite element, analytical and experimental studies, J. Acoust. Soc. Am. 112 (2002) 2589–2601.
[60] M.A. Fakih, S. Mustapha, M. Harb, C.-T. Ng, et al., Understanding the interaction of the fundamental Lamb-wave modes with material discontinuity: Finite element analysis and experimental validation, Struct. Health Monit. 21 (2022) 640–665.
[61] J.C.P. McKeon, M.K. Hinders, et al., Lamb wave scattering from a through hole, J. Sound Vib. 224 (1999) 843–862.
[62] M. Rebillat, M. Guskov, E. Balmes, N. Mechbal et al., Simultaneous influence of static load and temperature on the electromechanical signature of piezoelectric elements bonded to composite aeronautic structures, J. Vibr. Acoust. vol. 138, 2016.
[63] C. Fendzi, M. Rebillat, N. Mechbal, M. Guskov, G. Coffignal, et al., A data-driven temperature compensation approach for Structural Health Monitoring using Lamb waves, Struct. Health Monit. 15 (2016) 525–540.
[64] C. Nicard, M. Rébillat, O. Devos, M. El May, F. Letellier, S. Dubent, M. Thomachot, M. Fournier, P. Masse, N. Mechbal "COQTEL dataset: Corrosion Quantification Through Extended use of Lamb waves" 10.5281/zenodo.14193335.